Astronomy & Astrophysics manuscript no. main
December 6, 2022

Solar activity relations in energetic electron events measured by the MESSENGER mission

L. Rodríguez-García[1], L. A. Balmaceda[2,3], R. Gómez-Herrero[1], A. Kouloumvakos[4], N. Dresing[5], D. Lario[3], I. Zouganelis[6], A. Fedeli[5], F. Espinosa Lara[1], I. Cernuda[1], G. C. Ho[4], R. F. Wimmer-Schweingruber[7], and J. Rodríguez-Pacheco[1]

[1] Universidad de Alcalá, Space Research Group, Alcalá de Henares, Madrid, Spain
e-mail: l.rodriguezgarcia@edu.uah.es
[2] Heliophysics Science Division, NASA Goddard Space Flight Center, Greenbelt, MD, USA
[3] George Mason University, Fairfax, VA, USA
[4] The Johns Hopkins University Applied Physics Laboratory, 11101 Johns Hopkins Road, Laurel, MD 20723, USA
[5] Department of Physics and Astronomy, University of Turku, FI-20014 Turku, Finland
[6] European Space Astronomy Center, European Space Agency, Villanueva de la Cañada, Madrid, Spain
[7] Institut fuer Experimentelle und Angewandte Physik, University of Kiel, Kiel, Germany

Received December 1, 2022

ABSTRACT

Aims. We perform a statistical study of the relations between the properties of solar energetic electron (SEE) events measured by the MESSENGER mission from 2010 to 2015 and the parameters of the respective parent solar activity phenomena to identify the potential correlations between them. During the time of analysis MESSENGER heliocentric distance varied between 0.31 and 0.47 au.

Methods. We used the published list by Rodríguez-García et al. (2022) of 61 SEE events measured by MESSENGER, which includes the information of the near-relativistic electron peak intensities, the peak-intensity energy spectral indices, and the measured X-ray peak intensity of the flares related to the SEE events. Taking advantage of multi-viewpoint remote sensing observations, we reconstructed, whenever possible, the associated coronal mass ejections (CMEs) and shock waves; and we determined the 3D properties (location, speed, and width) of the CMEs and the maximum speed of the 3D CME-driven shocks in the corona. We used different methods (Spearman, Pearson, and a Bayesian approach, namely the Kelly method to linear regression) to estimate the correlation coefficients between the flare intensity, maximum speed at the apex of the CME-driven shock, CME speed at the apex, and CME width with the electron peak intensities and with the energy spectral indices. In this statistical study, we considered and addressed the limitations of the particle instrument on board MESSENGER (elevated background intensity level, anti-Sun pointing).

Results. We analysed both the full sample of events and the subsample of well-connected events, namely for -65° ≤ connection angle (CA) ≤ +33°, where the CA is the angular distance between the footpoint of the magnetic field connecting to the spacecraft and the longitude of the source region. For the well-connected sample, we find moderate to strong correlations between the near-relativistic electron peak intensity and both the 3D CME-driven shock maximum speed at the apex (Pearson: cc=0.65±0.04; Kelly: cc=0.87±0.20) and the flare peak intensity (Pearson: cc=0.59±0.03; Kelly: cc=0.74±0.30). When including poorly-connected events (full sample), the relations between the peak intensities and the solar activity phenomena are blurred, showing lower correlation coefficients.

Conclusions. (1) In this particular sample of events, with a majority of SEE events being widespread in heliolongitude and displaying relativistic electron intensity enhancements, a shock-related acceleration mechanism might be more relevant than a flare-related process in the acceleration of near-relativistic electrons. This result is mainly based on the stronger and more significant correlation found between the SEE peak intensities and the shock speed in comparison to the flare intensity; and on the asymmetry to the east of the range of connection angles for which the SEE events present higher peak intensities and higher correlations with the solar activity, which might be related to the evolution of the magnetic field connection to the shock front. (2) The correlations between the peak intensity of the SEE event and the shock speed or the flare intensity are stronger than in previous studies using measurements by spacecraft near 1 au.

Key words. Sun: particle emission– Sun: coronal mass ejections (CMEs) –Sun: flares – Sun: corona – Sun: heliosphere

1. Introduction

Solar energetic electron (SEE) events are sporadic enhancements of electron intensities associated to solar transient activity. In the inner heliosphere, these intensity enhancements are usually measured in situ at near-relativistic (≳ 30 keV) and relativistic (≳ 0.3 MeV) energies. The mechanisms proposed to explain the origin of solar near-relativistic electron events include: (1) acceleration during magnetic reconnection processes associated to solar jets (Krucker et al. 2011) and flares (Kahler 2007); (2) acceleration during magnetic restructuring in the aftermath of coronal mass ejections (CMEs) and in the current sheets formed at the wake of CMEs (e.g. Kahler & Hundhausen 1992; Maia & Pick 2004; Klein et al. 2005); (3) and/or acceleration at shocks driven by fast CMEs (Simnett et al. 2002).

Previous statistical studies point out that multiple acceleration processes may contribute to the acceleration of quasi-

relativistic energetic electrons (e.g. Kouloumvakos et al. 2015; Trottet et al. 2015). In particular, Trottet et al. (2015) concluded that near-relativistic electrons (~175 keV) in large SEP events have a mixed flare-CME origin, supported by Dresing et al. (2022) conclusions: electrons in the MeV range are mainly accelerated by CME-driven shocks, while lower energy (~50 keV) electrons are likely produced by a mixture of flare and shock-related acceleration processes.

Many efforts have been made to identify a unique accelerator by proving preferential correlations and analytical expressions between solar energetic particle (SEP) parameters, especially their peak intensity, and the properties of the associated solar activity phenomena, such as the solar flare X-ray peak intensity, CME speed and width, and CME-driven shock speed (e.g. Kahler 2001; Richardson et al. 2014; Papaioannou et al. 2016; Kouloumvakos et al. 2019; Xie et al. 2019; Kihara et al. 2020). The aforementioned studies are mainly based on measurements near 1 au, however particle propagation in the interplanetary space affect SEE properties. Thus, the observation of SEE events by spacecraft located at heliocentric distances less than 1 au (i.e., closer to the acceleration site) is essential to infer the mechanisms associated to their acceleration (e.g. Agueda & Lario 2016). To minimize projection effects in the CME properties and in the CME-driven shock speed, forward modelling is generally used to reconstruct the three-dimensional (3D) morphology of the CME and CME-driven shock in the corona, using imaging observations from multiple vantage points (e.g. Kwon et al. 2014; Kouloumvakos et al. 2016).

In this paper we study the relationship between solar activity (flare, CME, CME-shock) and the properties of SEE events measured by the *MErcury Surface Space ENvironment GEochemistry and Ranging* (MESSENGER; Solomon et al. 2007) mission near 0.3 au, presented by Rodríguez-García et al. (2022), hereafter Paper I. In particular, we use energetic electron measurements from 2010 February to 2015 April when MESSENGER's heliocentric distance varied between 0.31 and 0.47 au. We take advantage of the good remote-sensing coverage from near 1 au spacecraft, such as the twin spacecraft of the *Solar TErrestrial RElations Observatory* (STEREO; Kaiser et al. 2008) and the *SOlar and Heliospheric Observatory* (SOHO; Domingo et al. 1995), to reconstruct the 3D CMEs and CME-driven shocks associated to the SEE events. These multi-point observations allow us to study the relations between the solar source parameters and the peak intensity and peak-intensity energy spectrum of SEE events closer to the Sun.

Thus, the main goal of the study is to relate the peak intensities and peak-intensity energy spectra to various parameters of the parent solar activity, presented in Sect. 5. The rest of the paper is structured as follows. The instrumentation used in this study is introduced in Sect. 2. A summary of the SEE events measured by MESSENGER that were presented in Paper I is shown in Sect. 3. We include in Sect. 4 the 3D reconstructions of the CMEs and CME-driven shocks related to the SEE events. Section 6 summarizes and discusses the main findings of the study.

2. Instrumentation

The statistical study of the relations between SEE events and their parent solar source requires the analysis of both remote-sensing and in situ data from a wide range of instrumentation on board different spacecraft. We used data from MESSENGER, STEREO, SOHO, the *Solar Dynamics Observatory* (SDO; Pesnell et al. 2012), and the *Geostationary Operational Environmental Satellites* (GOES; García 1994).

Remote-sensing observations of CMEs and related solar activity phenomena on the Sun's surface were provided by the Atmospheric Imaging Assembly (AIA; Lemen et al. 2012) on board SDO, the C2 and C3 coronagraphs of the Large Angle and Spectrometric COronagraph (LASCO; Brueckner et al. 1995) instrument on board SOHO, and the Sun Earth Connection Coronal and Heliospheric Investigation (SECCHI; Howard et al. 2008) instrument suite on board STEREO. In particular, we used the COR1 and COR2 coronagraphs and the Extreme Ultraviolet Imager (EUVI; Wuelser et al. 2004), part of the SECCHI suite.

In Paper I, data from the X-Ray telescopes of the GOES satellites[1] and in situ energetic particle observations provided by the Energetic Particle Spectrometer (EPS), part of the Energetic Particle and Plasma Spectrometer (EPPS; Andrews et al. 2007) on board MESSENGER, were used.

3. SEE events measured by MESSENGER

The SEE events included in this study are presented in Paper I, where the data source and selection criteria are explained in detail. We summarize here the more relevant information.

3.1. Data source and SEE event selection criteria

The study includes MESSENGER data from 2010 February 7 to 2015 April 30. In this period, coinciding with most of the rising, maximum, and early decay phase of solar cycle 24, MESSENGER's heliocentric distance varied from 0.31 to 0.47 au.

The EPS instrument on board MESSENGER measured electrons from ~25 keV to ~1 MeV. The electron energies chosen in Paper I for the SEE event identification and statistical analysis were 71-112 keV. In the case of the analysis of energy spectra, the energies used were from ~71 keV to ~1 MeV divided into six energy bins. The EPS instrument was mounted on the far-side of the spacecraft, with a field of view divided into six sectors pointing in the antisunward direction, so it mostly detected particles moving sunward. Usually, SEP events present a higher particle flux and earlier onset in the sunward-pointing telescope that is aligned with the IP magnetic field (e.g. Kunow et al. 1991). Therefore, MESSENGER observations presumably provide a lower limit to the actual peak intensities of the SEE events and an upper limit to the timing of occurrence of such peaks.

The peak intensity in the prompt component of the event, namely the maximum intensity reached shortly (usually $\lesssim$6 hours) after its onset, was chosen as the maximum intensity. Although electron intensity enhancements associated to the passage of IP shocks are rare (Lario et al. 2003; Dresing et al. 2016), by selecting the prompt component of the SEE events, the possible effect that traveling IP shocks might have on the continuous injection of particles was minimized. Therefore, the peak intensity of the SEE events was observed when the associated CMEs were still close to the Sun.

Due to the elevated background level of the EPS instrument, the selected events showed intensities that are normally above $\sim 10^4$ (cm^2 sr s MeV)$^{-1}$. An exception to this is the period of 2011 August, when EPS geometric factor was modified allowing for a temporary detection of less intense events. In order to keep the self-consistency of the analysis, events number 6 and

[1] https://satdat.ngdc.noaa.gov/sem/goes/data/avg/

7, measured in August 2011 during the period of increased geometric factor of the MESSENGER/EPS instrument, were not included in this study.

3.2. MESSENGER SEE event list

Table A.1 shows the list of the 61 SEE events presented in Paper I. Columns 1-3 identify each SEE event with a number (1), the solar event date (2), and the time of the type III radio burst onset (3). The symbol (^) is used to indicate when the type III burst onset time is uncertain due to occultation or multiple radio emissions at the same time during the onset of the event. Column 4 provides the location of the solar flare in Stonyhurst coordinates, either identified in Paper I or consulted in different catalogues and studies (table 2 of Paper I). The flare class indicated in square brackets is based on the 1-8 Å channel measurements of the X-Ray telescopes on board GOES. To be consistent with previous statistical studies (e.g. Richardson et al. 2014), the flare location was chosen as the site of the putative particle source. Columns 5-7 are described in Sect. 4.

Column 8 in Table A.1 shows the MESSENGER connection angle (CA), which is the longitudinal separation between the flare site location and the footpoint of the magnetic field line connecting to the spacecraft, based on a nominal Parker spiral, as discussed below. Positive CA denotes a flare source located at the western side of the spacecraft's magnetic footpoint. The magnetic footpoint for MESSENGER was estimated assuming a Parker spiral with a constant speed of 400 km s^{-1} using the *Solar-MACH tool* available online[2] (Gieseler et al. 2022; Gieseler et al. 2022), as MESSENGER lacks solar wind measurements. The heliocentric distance of the MESSENGER spacecraft at the time of the event is given in Col. 9, which varied between 0.31 au and 0.47 au during the time interval considered in the study. Column 10 summarizes the 71-112 keV electron peak intensities corresponding to the prompt component of the event as discussed above. The pre-event background level is given in parentheses.

An event was considered widespread when either the MESSENGER |CA| is more than 80° or the longitudinal separation between MESSENGER and another spacecraft near 1 au that detected the event was more than 80° (Dresing et al. 2014). We indicate these events with (*) next to the event number in Col. 1 of Table A.1. A total of 44 SEE events can be characterized as widespread according to our criteria. However, the number of widespread events could be larger since, apart from not sampling all the heliolongitudes with the existing constellation of spacecraft, there were events with a high prior-event-related background or with no data available for some of the spacecraft, so no particle increase could be measured.

As detailed in Sect. 4, we found a CME (CME-driven shock) related to the electron increase in 57 (56) events. For these associations we previewed the available conoragraphic data from SOHO/LASCO or STEREO/COR2 near the flare and SEE onset times and register the related events. In almost all the cases, the CMEs and CME-driven shock waves were very prominent and clearly related to the flare eruption. Relativistic (~1 MeV) electron intensity enhancements were observed in 37 events, as indicated with (†) in Column 11 of the list. Thus, the majority of the events detected by MESSENGER are CME and CME-driven shock-related events, with a high peak intensity level and the presence of ~1 MeV electrons, which were observed by widely separated spacecraft. The observed characteristics of the SEE events are expected due to the high background level of MESSENGER/EPS that prevents the instrument from measuring less intense events (e.g. figure 1 in Lario et al. 2013).

4. Solar parent activity in SEE events measured by MESSENGER

To investigate the relations between the properties of the SEE events and some of the parent solar source parameters, we used the flare peak intensity measurements presented in Paper I for the events originating on the visible side of the Sun from Earth's point of view. The flare class based on GOES Soft X-ray (SXR) peak flux is given in square brackets in Col. 4 of Table A.1. For the far-side event #36 (2013/08/19), the equivalent GOES intensity of the flare is given using the STEREO/EUVI light curve (Nitta et al. 2013), as explained in Rodríguez-García et al. (2021) and indicated with (§) in Col. 4. The uncertainty of the logarithm of the flare intensity is estimated to be 0.1 W m^{-2}, taken as the rounding error of the measurements.

In this study we performed the 3D reconstruction of the associated CMEs and CME-driven shocks for 57 and 54 SEE events, respectively. In two events where a CME-driven shock was observed, we did not perform the 3D reconstruction as we could not trace the shock accurately. By determining the CME parameters, such as the width and speed, and the CME-driven shock speed from the 3D reconstruction, we reduced the projection effects and the final values are more accurate. Previous studies (e.g. Kouloumvakos et al. 2019; Xie et al. 2019; Dresing et al. 2022) show that when using in the statistical analysis the reconstructed parameters, instead of the plane-of-sky values, the estimated correlations are stronger. The reconstruction process is explained below.

4.1. 3D CME parameters

We took advantage of the multi-view spacecraft observations and reconstructed the 3D CME using the graduated cylindrical shell (GCS) model (Thernisien et al. 2006; Thernisien 2011). The GCS model uses the geometry of what looks like a hollow 'croissant' to fit a flux-rope structure using coronagraph images from multiple viewpoints. The deviations in the parameters of the GCS analysis are given in table 2 of Thernisien et al. (2009). The tools used for the reconstruction are (1) the *rtsccguicloud.pro* routine, available as part of the *scraytrace* package in the SolarSoft IDL library[3] and (2) *PyThea*, a software package to reconstruct the 3D structure of CMEs and shock waves (Kouloumvakos et al. 2022) written in Python and available online[4]. The images underwent a basic process of calibration, and we used base-difference images to highlight the CME contour from other coronal features. As inferred from the on-disk observations of the post-eruptive loops and/or of the filament prior to the eruption, several events (10 out of 57) showed non-radial propagation or presented 'curved axes'. This last term was introduced by Rodríguez-García et al. (2022) to refer to flux ropes that may deviate from the nominal semi-circular (croissant-like) shape and have instead an undulating axis. In these cases, the GCS parameters are chosen to better describe the portion of the CME closer to the ecliptic plane, which is closer to MESSENGER's orbit plane. Then, we obtained the following 3D CME parameters from the GCS reconstruction, as detailed by Thernisien et al. (2006); Thernisien (2011): (1) the *half-angle*; (2) the *ratio*, which sets the rate of lateral expansion of the minor radius

[2] https://doi.org/10.5281/zenodo.7100482

[3] http://www.lmsal.com/solarsoft/

[4] https://doi.org/10.5281/zenodo.5713659

to the height of the center of the CME at the apex; and (3) the *tilt*, which is the angle of the main axis of the CME relative to the solar equator.

The 3D CME speed at the apex and the CME width are given in Cols. 5 and 6 of Table A.1. The CME speed at the apex is derived from a linear fit of the different heights of the CME apex observed at different times taking at least three instants for the fitting. The uncertainty of the CME speed is considered to be 7% of the value, based on Kwon et al. (2014). The width of the CME was estimated based on Dumbović et al. (2019), where the angular extent in the equatorial plane is represented by $R_{maj} - (R_{maj} - R_{min}) \times |tilt|/90$. The value of R_{maj} (face-on CME half-width) was calculated by adding R_{min} (edge-on CME half-width) to the half-angle. The R_{min} was determined as the arcsin(*ratio*), which is given by GCS, as presented above. The uncertainty of the CME width in the equatorial plane is taken as the deviations of the half-angle given by Thernisien et al. (2009).

All the reconstructions were performed using three points of view (STEREO-A, -B and SDO and/or SOHO), whenever possible. For the reconstructions of events #54 and from number 58 to 61 we only used data from the Earth point-of-view, indicated with (!) in the Cols. 5 and 6 of Table A.1. These events occurred near the time of the solar superior conjunction of the STEREO spacecraft (from January to August 2015) and no STEREO data were available. However, these events are still included in the statistical study, keeping in mind that the reconstructed parameters could have larger uncertainties. After an exhaustive inspection of the data, we found no CME associated with events number 35, 42, 46, and 47.

4.2. 3D CME-driven shock speed

We also performed a reconstruction of the coronal shock waves associated to the SEE events, fitting an ellipsoid shape to the observations, although the actual shape of the outermost wave usually observed in front of the CME probably may differ from the assumed ideal contour. In order to do this, we used the *PyThea*[4] tool, which applies the ellipsoid model developed by Kwon et al. (2014) to quasi-simultaneous images from different vantage points. In this case, we used running-difference images to highlight the shock front in the calibrated images. The fitting process is explained in detail by Kwon et al. (2014) and by Kouloumvakos et al. (2019). We found no CME-driven shock for events number 30, 35, 42, 46 and 47. They are related to one slow CME (#30) and the four CME-less events discussed above. In events number 58 to 60 we used only data from the Earth point-of-view, indicated with (!) in the Cols. 7 of Table A.1, due to the lack of STEREO imaging during the solar superior conjunction, as discussed above. For events #54 and #61, it was not possible to constrain the CME-driven shock apex location due to the lack of STEREO imaging, indicated with (NP) in the list.

The coronal shocks usually accelerate at the formation phase, reach their maximum speed between ~3-10 $R_\odot$, and near ~10-15 $R_\odot$ they start the deceleration phase. Column 7 of Table A.1 shows the maximum speed of the 3D CME-driven shock at the apex, based on the 3D shock reconstruction using a spline fitting to the ellipsoid parameters over time. The uncertainty of the CME-driven shock speed is considered to be 8% of the value, following Kwon et al. (2014). In a few events (7 out of 54) the CME-driven shock speed is just smaller than the CME speed but within the uncertainties of the reconstructed parameters. This discrepancy is related to the uncertainty of the fitting process for both the CME and the shock; and to the differences in the fitting technique used for the CME-driven shock kinematics estimation, which uses spline fits to the geometrical parameters, as explained by Kouloumvakos et al. (2019) and by Kouloumvakos et al. (2022).

5. Relations between SEE parameters and the properties of their parent solar source

In this section, we present the relations between the SEE peak intensities and peak-intensity energy spectra and the properties of their parent solar activity for the events measured by MESSENGER. In particular, we compare the SEE events with the X-ray flare characteristics (location, peak intensity), with the 3D kinematic (speed) of the CME and of the CME-driven shock, and with the geometric parameters (width) of the CME, when possible. For this purpose, we use two different probability approaches to apply an appropriate method of correlation between the variables, addressing the instrumental limitations (elevated background level, anti-Sun pointing) of the particle instrument on board MESSENGER.

5.1. Frequentist probability approach: Spearman and Pearson correlation coefficients

There are several methods to approach the correlation between variables, such as Spearman or Pearson techniques. The Spearman rank correlation coefficient (Spearman 1987) is often used as a statistical test to determine if there is a relation between two random variables. As a nonparametric rank-based correlation measurement, it can also be used with nominal or ordinal data. The associated statistical test does not need any hypothesis about the shape of the distribution of the population from which the samples are taken (Kokoska & Zwillinger 2000). In contrast, the Pearson correlation method (Kowalski 1972) assumes bivariate normal distribution for the variables. Then, while Pearson correlation provides a complete description of the association when the assumption is fulfilled, conclusions based on significance testing may not be robust in the case of non-bivariate normality. Thus, before using the generally known Pearson method in the association of the variables, we characterized the samples to assess whether assumption of normality is acceptable or not. For this purpose, a combination of visual inspection, assessment of the skewness and kurtosis (West et al. 1995), and formal normality tests (D'Agostino & Pearson 1973; Stephens 1974) were used. We note that, for the variables included in this study, taking logarithms usually transforms a non-Gaussian-like distribution into normality.

Table 1 presents a statistics summary of the samples for each of the parameters of interest, listed in Col. 1. As discussed above, we used the logarithm of the variables in the majority of the parameters to work with normally distributed data. We divided each of the samples into two subsamples (rows): the full sample of events and the sample where the connection angle is -65° ≤ CA ≤ 33°. This subsample of events is chosen as the well-connected events, as detailed in Sect. 5.3.1. Columns 2-9 show the count, the mean, the standard deviation (STD), the minimum, the 25, 50 (median), 75 percentile marks, and the maximum values, respectively. Column 10 shows the skewness of the sample, which measures the lack of symmetry. Positive (negative) skewness corresponds to right (left) skewed sample relative to a normal distribution. Column 11 presents the kurtosis value, which measures whether the data are heavy-tailed (kurtosis>3) or light-tailed (kurtosis<3) relative to a normal distribution. Columns 12-

Table 1. Summary of the statistical properties of the different samples analysed in this study.

Variable		Count	Mean	STD	Min	25%	50%	75%	Max	Skew	Kurt	Zskew	Zkurt	Normal
(1)		(2)	(3)	(4)	(5)	(6)	(7)	(8)	(9)	(10)	(11)	(12)	(13)	(14)
Log Peak Int	all	59	5.09	0.93	3.77	4.41	4.79	5.44	7.69	1.29	3.93	3.66, 0.00	1.63, 0.10	No
	(w-con)	(30)	(5.41)	(1.05)	(3.77)	(4.58)	(5.21)	(6.04)	(7.69)	(0.76)	(2.71)	(1.87, 0.06)	(0.08, 0.93)	(Yes)
Log Flare Int	all	38	-4.5	0.75	-6.32	-5.03	-4.35	-3.93	-3.27	-0.53	2.58	-1.47, 0.14	-0.27, 0.79	Yes
	(w-con)	(18)	(-4.62)	(0.81)	(-6.32)	(-5.15)	(-4.59)	(-3.97)	(-3.27)	(-0.26)	(2.29)	(-0.57, 0.57)	(-0.41, 0.68)	(Yes)
Log Shock Spe	all	52	3.22	0.15	2.90	3.10	3.21	3.35	3.53	0.18	2.32	0.59, 0.55	-1.14, 0.25	Yes
	(w-con[1])	(24)	(3.23)	(0.15)	(3.04)	(3.13)	(3.17)	(3.27)	(3.53)	(0.92)	(2.69)	(2.04, 0.04)	(0.12, 0.90)	(Yes)
Log CME Spe	all	55	3.08	0.20	2.41	2.96	3.11	3.23	3.43	-0.81	3.9	-2.47, 0.01	1.57, 0.11	Yes
	(w-con)	(26)	(3.07)	(0.22)	(2.41)	(2.97)	(3.08)	(3.19)	(3.43)	(-0.97)	(4.62)	(-2.19, 0.03)	(1.98, 0.05)	(Yes)
Log CME Wid	all	55	1.83	0.15	1.36	1.74	1.84	1.89	2.20	-0.25	4.17	-0.83, 0.40	1.83, 0.07	Yes
	(w-con)	(26)	(1.85)	(0.14)	(1.66)	(1.75)	(1.82)	(1.89)	(2.20)	(0.95)	(3.20)	(2.15, 0.03)	(0.79, 0.43)	(Yes)
δ_{200}	all	42	-1.94	0.19	-2.56	-1.99	-1.92	-1.82	-1.55	-1.11	5.26	-2.88, 0.00	2.47, 0.01	No
	(w-con)	(23)	(-1.97)	(0.14)	(-2.41)	(-2.01)	(-1.94)	(-1.90)	(-1.81)	(-1.85)	(6.64)	(-3.47, 0.00)	(2.88, 0.00)	(No)

Notes. Column 1: Variables for the full sample and well-connected events (in parenthesis, namely -65° ≤ connection angle ≤ 33°) in the respectively following units: peak intensity (cm^2 sr s MeV)$^{-1}$, flare intensity (W m^{-2}), CME-driven shock speed (km s^{-1}), CME speed (km s^{-1}), CME width (deg), spectral index (-). Column 2: total number of entries. Column 3: Average of all entries. Column 4: Standard deviation. Column 5: minimum value. Columns 6-8: 25, 50 (median), and 75 percentile mark, respectively. Column 9: maximum value. Column 10: skewness, namely the measure of the lack of symmetry. Column 11: kurtosis, namely the measure of whether the data are heavy-tailed or light-tailed relative to a normal distribution. Column 12: Z-skewness: statistics, p-value. Column 13: Z-kurtosis: statistics, p-value. Column 14: Whether data can be considered normally distributed or not based on several criteria: visual inspection of the distribution, Z-value (both skewness and kurtosis; West et al. 1995), Normality test (not shown; D'Agostino & Pearson 1973), and Anderson-Darling test (not shown; Stephens 1974). [1] in Col. 1: Only the Anderson-Darling test (not shown; Stephens 1974) is not fulfilled.

Table 2. Spearman and Pearson correlations between the variables involved in this study.

	Log Flare Intensity Spearman//Pearson	Log CME-driven shock speed Spearman//Pearson	Log CME speed Spearman//Pearson	Log CME width Spearman//Pearson
(1)	(2)	(3)	(4)	(5)
Log SEE Peak Intensity	0.32±0.04//–	0.26±0.04 //–	0.23±0.03 //–	0.21±0.04 //–
(well-connected events)*	(–//0.59±0.03)	(–//0.65±0.04)	(–//0.46±0.03)	(–//0.26±0.04)
Log Flare Intentsity	-	–//0.53±0.04	–//0.57±0.03	–//0.22±0.05
Log CME-driven shock Speed	-	-	–//0.81±0.02	–//0.23±0.04
Log CME Speed	-	-	-	–//0.26±0.04

Notes. * in Col. 1: correlations given for the subsample of well-connected events: -65° ≤ connection angle ≤ 33°).

13 show the results (stats, p-value) of the Z-tests for the skewness and the kurtosis (e.g. West et al. 1995).

Then, based on the criteria discussed above, we list (Yes) in Col. 14 if the data can be considered normally distributed and (No) if the data show substantial departure from normality, invalidating conventional statistical tests that assume Gaussian distribution (such as, for instance, when estimating the Pearson correlation coefficient). Therefore, in the following we use the Spearman (Pearson) correlation for the samples with No (Yes) in Col. 14 of Table 1. When calculating the correlations, to estimate the statistical uncertainty, namely the confidence intervals of the correlation coefficients derived from the samples, and the uncertainties of the p-value related to the coefficients, we used the Monte Carlo method (e.g. Wall & Jenkins 2003; Curran 2015): the correlation coefficient and p-value are calculated for N pairs of values chosen at random within the set of N observations and the respective measurement errors. This procedure is repeated n = 10000 times.

Furthermore, to characterize the logarithm of the electron peak intensity population in an unbiased fashion, we should address the limitations of the particle instrument on board MESSENGER. The intensity of the SEE events is truncated at the sensitivity limit (background level) of the EPS instrument, which is close to ~10^4 (cm^2 sr s MeV)$^{-1}$, indicated with the horizontal lines in Fig. 1. The truncation indicates that the undetected events are entirely missing from the dataset. This truncation might affect the shape of the distribution of the sample, which can departure from normality and bias the correlation analysis

Table 3. Correlations between the variables involved in this study based on the Kelly method.

	Log Flare Intensity	Log CME-driven shock speed	Log CME speed	Log CME width
(1)	(2)	(3)	(4)	(5)
Log SEE Peak Intensity	0.56 ± 0.38	0.68±0.33	0.47 ± 0.43	0.52 ±0.36
(well-connected events)*	(0.74 ± 0.30)	(0.87 ± 0.20)	(0.60 ± 0.39)	(0.27 ± 0.44)
Log Flare Intensity	-	0.60 ± 0.12	0.61 ± 0.11	0.25 ± 0.14
Log CME-driven shock speed	-	-	0.88 ± 0.04	0.27 ± 0.12
Log CME speed	-	-	-	0.28 ± 0.11

Notes. * in Col. 1: correlations given for the subsample of well-connected events: -65° ≤ connection angle ≤ 33°).

when not properly accounted. Thus, we addressed the truncation characterizing the sample to choose the appropriate correlation method, namely Spearman or Pearson. In addition, due to the anti-Sun pointing of the EPS instrument, MESSENGER observations presumably provide a lower limit to the actual peak intensities of the SEE events. To address this fact, we used the median value of the relation between the intensities of the antisunward and sunward propagating particles, deduced in Paper I using Solar Orbiter data when the spacecraft's radial distance from the Sun ranged from 0.34 to 0.83 au: (I_{max_sun}/I_{max_asun}=1.3±0.5). Thus, to estimate the correlation coefficient we included the maximum deviation of I_{max_sun}/I_{max_asun}=1.8 in the error of the data points used in the Monte Carlo method discussed above. We note that the SEE peak intensities have asymmetric errors. They may take any value from the measured intensity up to the multiplying factor of 1.8 on the measured intensity.

5.2. Bayesian probability approach: Kelly method

We also estimated the correlation coefficients between the different variables included in this study using the Bayesian approach by Kelly (2007), hereafter the Kelly method. Bayesian inference belongs to the category of evidential probabilities: to evaluate the probability of a hypothesis, the *prior* distribution is specified for each statistical parameter which quantifies the prior knowledge on the possible values. This, in turn, is subsequently updated to a *posterior* probability distribution in the light of new, relevant data (evidence). The Bayesian interpretation provides a standard set of procedures and formulae to perform this calculation. In the Kelly method, a generalized likelihood function for the measured data is constructed and the intrinsic distribution of the independent variables is approximated using a mixture of Gaussian functions instead of using predetermined model distributions. This approach differs from the ones discussed in the previous section and offers a more robust alternative to the commonly used ordinary least-squares (OLS) methods as it directly accounts for: (1) measurement errors in both, the independent and dependent variables in linear regression; (2) intrinsic scatter; and (3) selection effects such as nondetections (e.g. censored or truncated data) (Kelly 2007; Feigelson & Babu 2012). In the following we present the results using both methods, namely the Spearman/Pearson correlations and the Kelly approach.

5.3. SEE peak intensity versus solar activity parameters

In this section we followed the procedure presented above to estimate the correlations between the SEE peak intensity and the parameters related to their parent solar activity. The different correlation coefficients found in this study are summarized in Table 2 (Spearman and Pearson methods) and Table 3 (Kelly method). The correlation coefficients based on the Kelly method listed in Table 3 are obtained as the median value from the posterior distribution presented above, while the uncertainty of the correlation corresponds to the median absolute deviation (MAD; Feigelson & Babu 2012). As detailed below, we note that the values for the correlation coefficients and uncertainties using the Kelly method are larger than the ones obtained using Spearman and Pearson methods. This is mainly due to the Kelly method including the measurement errors when estimating the correlation coefficients. We find a wider credible intervals when the correlations are less clear.

5.3.1. SEE peak intensity versus flare location

Figure 1a shows the 71-112 keV electron peak intensities as a function of the CA, which is the longitudinal separation between the flare location and the footpoint of the magnetic field connecting to the spacecraft, as discussed in Sect. 3.2. The events with the largest intensities, between ~10^5 and ~10^8 (cm^2 sr s MeV)$^{-1}$, are observed between -75° ≲ CA≲ +38°, including the well-connected events at CA~0°, with a trend toward negative CA values. We note the asymmetry in the positive and negative CAs. Based on the observed asymmetry, we divided the full sample into well- and poorly- connected events using the centroid ϕ_0 and sigma σ found by Lario et al. (2013). They used a Gaussian to describe the longitudinal distribution of peak intensities for spacecraft near 1 au. Lario et al. (2013) found, in the case of 71-112 keV electrons and using a constant speed of 400 km s^{-1} for the solar wind speed, that ϕ_0=-16°±3° and σ=49°±2°. Therefore we chose the connection angle interval CA ∈ -16°±49°(-65° ≤ CA ≤ +33°) as the well-connected sector. These SEE events are indicated in purple color in Fig. 1a. The green colored events in the figure include the poorly-connected events, which tend to have intensities below ~10^5 (cm^{2}sr s MeV)$^{-1}$. We note that we found a few higher-intensity events (3 out of 29) in the poorly-connected sample. The percentage of poorly-connected events included in the full sample is of ~45%. Figure 1b shows that for the majority (25 out 28) of the poorly-connected events the peak electron intensities ranges from ~10^4 to ~10^5 (cm^{2}sr s MeV)$^{-1}$, independently of the CME-driven shock speed associated to the SEE event. The horizontal lines in Fig. 1 show the truncation level of the sample, related to the elevated background of the particle instrument, which is close to ~10^4 (cm^{2}sr s MeV)$^{-1}$, as discussed in Sect. 5.1.

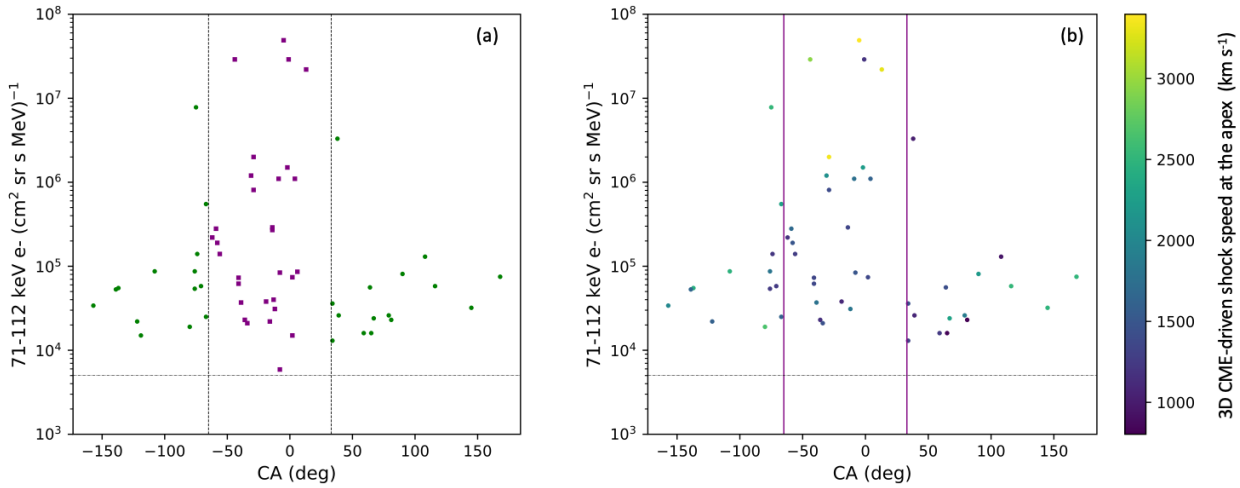

Fig. 1. MESSENGER solar energetic electron peak intensities versus the connection angle (CA). The vertical dashed lines indicate the connection angles CA=-65° (left) and CA=+33° (right). The horizontal lines show the truncation level of the sample. *(a)* Includes all SEE events selected for the study. The color of the points depends on the CA. The purple squared-shaped points correspond to the sample of well-connected events, namely -65° ≤ CA ≤ +33°. The rest of the sample is indicated with green circles. *(b)* Only events accompanied by a CME-driven shock are shown, which are color-coded by the shock speed at the apex.

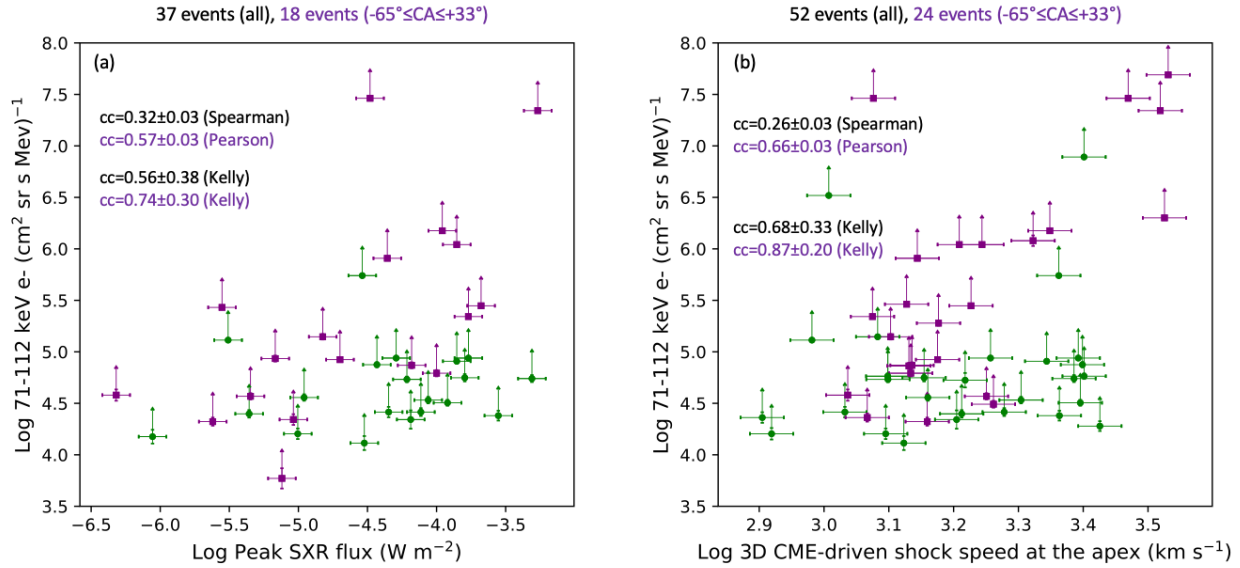

Fig. 2. Logarithm of the electron peak intensity against the logarithm of the flare intensity (*a*) and the logarithm of the 3D CME-driven shock maximum speed at the apex (*b*). The color code of the points is the same as in Fig. 1a. All the points show the error bars corresponding to the uncertainties of the measurements. The vertical arrows over the points represent the error due to the anti-Sun pointing of the EPS instrument. The legend shows the number of events and the correlation coefficients corresponding to the full (well-connected) events in black (purple). Details given in the main text.

5.3.2. SEE peak intensity versus flare intensity

Figure 2a shows the logarithm of the 71-112 keV electron peak intensities plotted against the logarithm of the flare SXR peak flux. The points show the error bars corresponding to the uncertainties of the measurements. The vertical arrows indicate the error in the measured SEE peak intensities due to the anti-Sun pointing of the EPS instrument, as discussed in Sect. 5.1. The color code of the points is the same as in Fig. 1a. The number of events included in the full sample and well-connected events are given on the top of the panel and in Col. 2 of Table 1. The legend also shows the correlation coefficients for the two different approaches discussed above.

Column 2 of the first row in Table 2 shows that the Spearman correlation between the logarithms of the peak SEE intensity and the flare intensity is weak: cc=0.32±0.04. This correlation is significantly higher than that (cc=0.12) found by Dresing et al. (2022) for a subsample of about 40 electron (55-85 keV) events measured near 1 au by STEREO. We note that that study also included both well- and poorly- connected events. The correlation between the SEE peak intensities and the flare intensity is significantly larger for the well-connected events, with a moderate Pearson correlation coefficient of cc=0.59±0.03. This value is in agreement with Trottet et al. (2015), who found a correlation of cc=0.53±0.09 for the 38 electron (175 keV) events in the

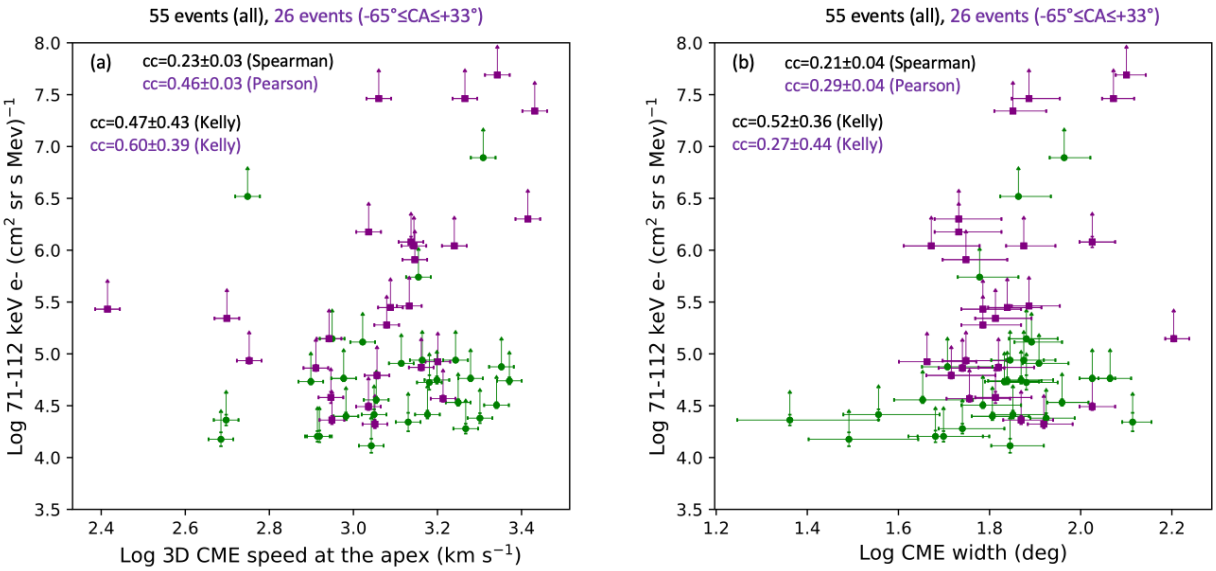

Fig. 3. Logarithm of the electron peak intensity against the logarithm of the 3D CME speed at the apex (*a*) and 3D CME width at the ecliptic plane (*b*). Colors and legend as in Fig. 2.

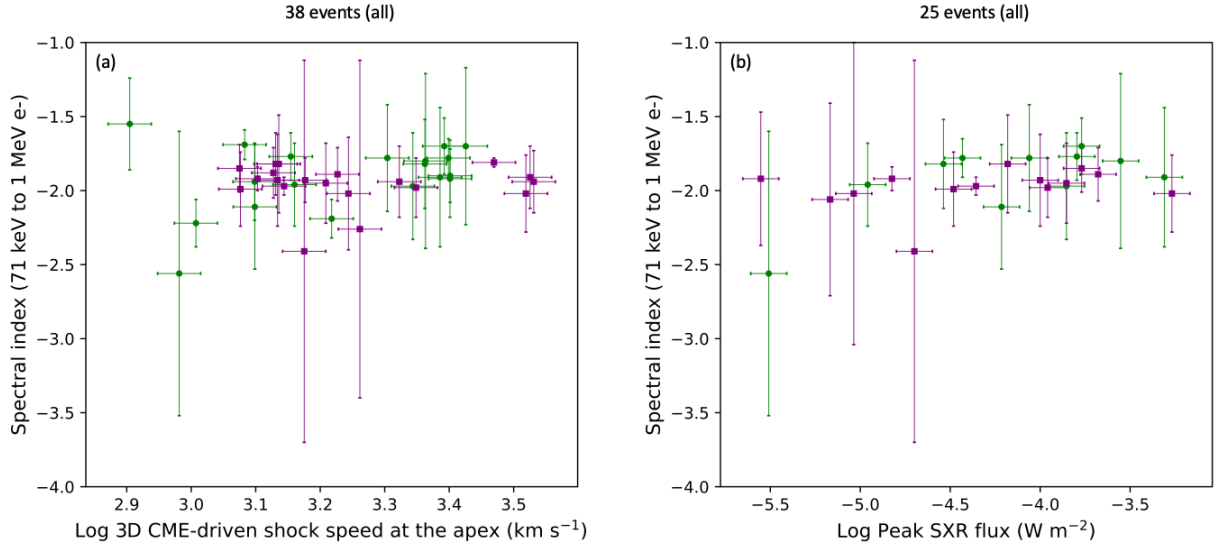

Fig. 4. MESSENGER solar energetic electron spectral indices against the CME-driven shock speed at the apex *(a)* and the SXR intensity of the flare *(b)*. The color code of the points as in Fig. 1a.

western solar hemisphere (CA≃0), measured near 1 au by the *Advanced Composition Explorer* (ACE; Stone et al. 1998).

Similarly, using the Kelly approach (first row, Col. 2, Table 3), the logarithm of the peak intensity shows lower correlation with the logarithm of the flare intensity for the full sample (cc=0.56±0.38) than for the well-connected events (cc=0.74±0.30). In contrast to Spearman and Pearson methods, the Kelly approach respectively gives a moderate (versus weak) and strong (versus moderate) correlation for both aforementioned samples.

5.3.3. SEE peak intensity versus CME-driven shock speed

Figure 2b shows the logarithm of the 71-112 keV electron peak intensities plotted against the logarithm of the 3D CME-driven shock maximum speed at the apex. Color code of the points as in Fig. 1a. Error bars and legend are similar to Fig. 2a. Column 3 of the first row of Table 2 shows that the Spearman correlation between the logarithms of the peak SEE intensity and the 3D CME-driven shock speed at the apex is low: cc=0.26±0.04. This correlation is similar to that (cc=0.24) found by Dresing et al. (2022) for the correlation between the logarithm of the peak intensities and the speed (not the logarithm) of the shock apex for a full sample of 33 electron (55-85 keV) events measured near 1 au by the two STEREO spacecraft. We note that Dresing et al. (2022) include both well- and poorly- connected events and also used 3D parameters of the coronal shock reconstruction, which resulted in larger correlation coefficients compared to not using 3D parameters.

In the case of well-connected events, indicated in Fig. 1b with the vertical purple lines, the correlation found in this study is significantly larger, with a moderate Pearson correlation coefficient of cc=0.65±0.04. This correlation is slightly higher than

that (cc=0.49) estimated by Xie et al. (2019) comparing the logarithm of the 62-105 keV electron peak intensities with the 3D shock speed (not the logarithm) for CA=0, from a sample of events measured during solar cycle 24 by STEREO and ACE.

Similarly, using the Kelly approach (first row, Col. 3, Table 3), the logarithm of the peak intensity shows lower correlation with the logarithm of the shock speed for the full sample (cc=0.68±0.33) than for the well-connected events (cc=0.87±0.20). In contrast to Spearman and Pearson methods, the Kelly approach respectively gives a strong (versus weak) and very strong (versus strong) correlation for both aforementioned samples. We note that the uncertainty for the well-connected events is smaller than for the full sample, therefore the significance of the correlation is larger.

5.3.4. SEE peak intensity versus CME speed

Figure 3a shows the logarithm of the 71-112 keV electron peak intensities versus the logarithm of the 3D CME speed at the apex. Color code of the points as in Fig. 1a. Error bars and legend are similar to Fig. 2. Column 4 of the first row in Table 2 shows that the correlation between the logarithms of the peak SEE intensity and the 3D CME speed at the apex is low: cc=0.23±0.03. This correlation is also significantly larger for the well-connected events, with a moderate Pearson correlation coefficient of cc=0.46±0.03. This value is slightly lower than that (cc=0.68±0.09) found by Trottet et al. (2015) for 38 electron (175 keV) events in the western solar hemisphere (CA≃0) measured near 1 au by ACE. We note that in that study the values of the CME speed were estimated from linear fits to the time-height trajectory of the CME front, as provided in the CME catalogue (Yashiro et al. 2004) of SOHO/LASCO. However, being limb events, the projected speed would not be significantly different from the actual 3D value.

Similarly, using the Kelly approach (first row, Col. 4, Table 3), the logarithm of the peak intensity shows lower correlation with the logarithm of the CME speed for the full sample (cc=0.47±0.43) than for the well-connected events (cc=0.60±0.39). We note that the correlation for the full sample is not significant, as the uncertainty is similar to the coefficient value. In contrast to Spearman and Pearson methods, the Kelly approach gives a strong (versus moderate) correlation for the well-connected sample. We note that in all the cases, the correlations found here are lower than that found for the CME-driven shock presented in Sect. 5.3.3.

5.3.5. SEE peak intensity versus CME width

Figure 3b shows the logarithm of the SEE peak intensity versus the logarithm of the 3D CME width in the ecliptic plane. Color code of the points as in Fig. 1a. Error bars and legend are similar to Fig. 2a. Column 5 of the first row in Table 2 shows that the correlation between the logarithms of the peak SEE intensity and the 3D CME width is low: cc=0.21±0.04. This value is in agreement with Kahler et al. (1999), who found a similar weak correlation (cc=0.28) between the angular width of the CME and the logarithm of the proton peak intensities. The correlation is not significantly larger for well-connected events, with a low Pearson correlation coefficient of cc=0.26±0.04.

Using the Kelly approach (first row, Col. 5, Table 3), the logarithm of the peak intensity shows higher correlation with the logarithm of the CME width for the full sample (cc=0.52±0.36) than for the well-connected events (cc=0.27±0.44). We note that the uncertainty is higher than the correlation coefficient in the case of the well-connected sample, so the correlation is not significant.

5.4. SEE peak-intensity energy spectra versus coronal shock speed and flare intensity

In Paper I, the peak-intensity energy spectra of 42 SEE events measured by the MESSENGER mission were analysed. The energies used in the analysis ranged from ~71 keV to ~1 MeV divided into six energy bins. For each of the events, they took the time-of- maximum based on the 71-112 keV channel using one-hour averages and read the intensity peak at this time for the rest of the energy channels. For all the events, the fitting resembled a single power-law, giving the spectral index and its uncertainty, δ200. Figures 4a and 4b show the spectral indices against the logarithm of the 3D CME-driven shock maximum speed at the apex and the logarithm of the flare intensity, respectively. The color code of the points is the same as in Fig. 1a. We find no correlation for any of them. This result is in agreement with Dresing et al. (2022), where no clear correlations are found between the shock parameters and the spectral indices of the near-relativistic electrons. We do not observe harder spectra with increasing peak intensities (not shown), as Kahler (2001) found for high energy protons (>10 MeV).

5.5. Relations between the solar parent activity

The last three rows of Table 2 and Table 3 show the correlations between the variables describing the solar activity. There is a moderate correlation between the logarithms of the flare intensity and the 3D CME-driven shock speed (Pearson: cc=0.53±0.04; Kelly: cc=0.60±0.12; 33 events) and the 3D CME speed (Pearson: cc=0.57±0.03, Kelly: cc=0.61±0.11; 36 events). This last value is similar to the correlation coefficient (Pearson: cc=0.66) obtained by Kihara et al. (2020) sampling 79 events from 2006 to 2014 with near 1 au spacecraft. We note that Kihara et al. (2020) use the CME speed instead of the logarithm of this variable. The correlation between the 3D CME-driven maximum shock speed and the 3D CME speed is strong (Pearson: cc=0.81±0.02; Kelly: cc=0.88±0.04; 52 events). There is a weak correlation between the 3D CME width and any of the other variables.

6. Summary and discussion

We used the list of 61 SEE events measured by the MESSENGER mission from 2010 to 2015, presented by Rodríguez-García et al. (2022) (Paper I), when the heliocentric distance of the spacecraft varied from 0.31 au to 0.47 au. Due to the elevated background intensity level of the particle instrument on board MESSENGER, the SEE events measured by this mission are necessarily large and intense; most of them are accompanied by a CME-driven shock, are widespread in heliolongitude, and display relativistic (~1 MeV) electron intensity enhancements. The largest peak intensities, between ~10^5 and ~10^8 (cm^2 sr s MeV)$^{-1}$, are observed in the range of connection angles -75° < CA < +38°, with an asymmetry to longitudes east of the well-connected longitudes CA ~ 0°.

To relate the near-relativistic electron peak intensity and the peak-intensity energy spectra to different parameters of the parent solar source, we (1) considered the flare peak intensity measured in Paper I from the events originating on the visible side

of the Sun from Earth's point of view and (2) took advantage of the multi-viewpoint spacecraft observations to reconstruct, when possible, the 3D large-scale structure of the CME and the CME-driven shock using the GCS model (Thernisien 2011) and the ellipsoid model (Kwon et al. 2014), respectively. We added some of the reconstructed parameters to the list of SEE events in Table A.1 for future reference.

6.1. Summary of observational results

In this work, we first characterized the distribution of the samples in order to select the appropriate method to estimate the correlation coefficients between the SEE peak intensity and energy spectra and several parameters related to the solar activity. We also addressed the fact that the peak intensities measured by MESSENGER were truncated and presented asymmetric uncertainties due to instrumental limitations (elevated background level, anti-Sun pointing). The observational results of this study are summarised as follows:

- There is an asymmetry in the positive and negative connection angles for which the largest intensities are measured. This asymmetry was, therefore, considered in the definition of the connection angle interval in the so-called well-connected events, namely -65° ≤ CA ≤ +33°, in which we found stronger correlations between the SEE peak intensities and the solar parameters in comparison to the full sample.
- In the majority of the poorly-connected events, the peak intensities are below ~10^5 (cm^2 sr s MeV)$^{-1}$, independently of the intensity of the flare or the speed of the CME-driven shock. A poor connectivity to the source weakens the correlations between the peak intensities and the different parent solar source parameters.
- The strongest correlations are found between the near-relativistic electron peak intensities and the maximum speed at the apex of the 3D CME-driven shock and the flare intensity for the so-called well-connected events. The Pearson correlation coefficients and their uncertainties based on a Monte Carlo method are: cc=0.65±0.04 (shock) and cc=0.59±0.03 (flare). We note a slightly higher correlation with the 3D CME-driven shock maximum speed at the apex than with the flare intensity. The correlation coefficients based on the Kelly method are cc=0.87±0.20 (shock) and cc=0.74±0.30 (flare). We also note the reduced uncertainty in the case of the shock sample compared to the correlations with other solar parameters.
- We find a moderate (strong) correlation between the near-relativistic electron peak intensities and the CME speed at the apex for the well-connected events, with a Pearson (Kelly) correlation coefficient of cc=0.46±0.03 (cc=0.60±0.39).
- The weakest correlations for the well-connected events are found between the near-relativistic electron peak intensities and the 3D CME width, with a Pearson (Kelly) correlation coefficient of cc=0.26±0.04 (cc=0.27±0.44). We note that in the Kelly method, the uncertainty is higher than the correlation coefficient, indicating that no significant correlation can be determined.
- The correlations between the near-relativistic electron peak intensities and the solar activity, namely the flare intensity and 3D CME-driven shock speed, estimated in this study are higher than that found by equivalent studies based on near 1 au measurements.
- We find no correlation between the spectral indices and the flare intensity nor the CME-driven shock speed.
- Correlations of similar order exist between the different parameters describing the solar activity, such as the flare intensity, the CME speed, or the CME-driven shock. In the case of the flare intensity and the shock speed, the correlation between the variables are smaller than the correlations between the SEE peak intensities and either the flare intensity or the shock speed.

6.2. Effect on the interpretation of the origin of SEEs

6.2.1. Correlations between the parameters characterising the solar activity

One of the difficulties found when interpreting statistical relations between solar activity and SEEs is the interrelationship of the different parameters utilized to characterise the solar activity, as summarized in the last three rows of Tables 2 and 3. For example, Kahler (1982) introduced the term Big Flare Syndrome to illustrate the observational fact that there is a correlation between any two parameters measuring the magnitude of a flare event, independent of the detailed physical relationship between them. In this study, we find a moderate correlation between the SXR peak flux and the CME speed (Pearson: cc=0.57±0.03; Kelly: cc=0.61±0.11). This correlation might be related to a common physical process at the Sun. It is well known that the acceleration of CMEs is closely related in time with the evolution of thermal energy release in the associated flare (Zhang et al. 2004; Bein et al. 2012), suggesting an interdependence between the CME speed and the peak flux of the flare.

As expected, we find a strong correlation between the maximum speed at the apex of the 3D CME-driven shock and the 3D CME speed at the apex derived from a linear fit of the time evolution of the CME apex height (Pearson: cc=0.81±0.02; Kelly: cc=0.88±0.04). This correlation might be expected to be even higher (i.e., closer to cc=1). A reason for the rather lower value we find could be related to measuring the maximum speed for the shock but the average linear speed for the CME. Lastly, we find a moderate correlation between the flare intensity and the 3D CME-driven shock speed (Pearson: cc=0.53±0.04; Kelly: cc=0.60±0.12), which might be related to both the intrinsic relation between the flare intensity and the CME speed, and the relation between the CME speed and the CME-driven shock speed, as discussed above.

Using partial correlations in the analysis of the relations between SEE parameters and the solar activity (e.g. Trottet et al. 2015) might be a simplification of the real picture, as the correlations between variables actually show a degeneracy in the parameter space. The flare-related and CME-related phenomena are expressions of the solar activity and it is very probable that both of them share the same common origin at the Sun. Furthermore, based on previous studies, it is probable that using different parameters to characterize the solar activity, such as the fluence for the flare activity (Trottet et al. 2015) or the CME-driven shock speed at the cobpoint (Heras et al. 1995) for the shock activity (Dresing et al. 2022), would increase the correlations with the peak intensities.

6.2.2. Correlation between SEE intensities and solar activity

Our study finds a distinct difference between the SEE correlations found for different samples, when classifying them by different connection angles. For the full sample of the events, including poorly connected events, we find similar weak Pearson correlations for the different quantities that describe the so-

lar activity, varying from cc ~0.21 to ~0.32. Also, the uncertainty found in the correlations based on the Kelly method are significant with respect to the correlation coefficient, meaning that the correlations are not clear. This results is expected due to the inclusion of the poorly-connected events in the study, where the transport effects and/or the connection to peripheral areas of the source (shock) could significantly distort the correlations. This behaviour is clearly observed in Fig. 1b, where the majority of the points outside the purple vertical lines, indicating the well-connected range, are showing intensities between ~10^4 and ~10^5(cm^2 sr s MeV)$^{-1}$ independently of the shock speed. The few high-intensity points outside the well-connected range might be related to varying CME widths and/or different footpoint locations caused by non-nominal solar wind speed or disturbed Parker-field.

However, for the well-connected events, namely for -65° ≤ CA ≤ 33°, we generally find clearer correlations. The SEE peak intensities correlate slightly better with the 3D CME-driven maximum shock speed (Pearson: cc=0.65±0.04; Kelly: cc=0.87±0.20) than with the SXR peak flux (Pearson: cc=0.59±0.03; Kelly: cc=0.74±0.30), and both better than with the CME speed (Pearson: cc=0.46±0.03; Kelly: cc=0.60±0.39). Thus, the correlation of the peak electron intensity is higher and also more significant with the 3D CME-driven shock maximum speed at the apex than with the CME speed at the apex. This means that the maximum shock speed might be a better proxy of the acceleration of energetic electrons than the linear CME speed.

For the well-connected events, we also found that the correlation between the logarithms of the peak intensity of the SEE events and the speed of the CME-driven shock at the apex is stronger in the SEE events measured by MESSENGER (Pearson: cc=0.65±0.04; Kelly: cc=0.87±0.20) in comparison to near 1 au data (Pearson: cc=0.49) for similar near-relativistic energies and using CME and associated 3D shock parameters (Xie et al. 2019). We note that Xie et al. (2019) use the speed of the shock instead of the logarithm of the shock speed. However, the results are similar comparing directly the shock speed in both studies. Similarly, the correlation between the peak intensities and the flare intensity for the full sample (Pearson: cc=0.32±0.04; Kelly: cc=0.56±0.38) is higher than that found for near 1 au measurements (Pearson: cc=0.12; Dresing et al. 2022), which included both well- and poorly- connected events. In the case of well-connected events (-65° ≤ CA ≤ 33°), we find similar correlations (Pearson: cc=0.59±0.03; Kelly: cc=0.74±0.30) as Trottet et al. (2015), using near 1 au data (Pearson: cc=0.53±0.09). However, that study is restricted to the western events measured by ACE, with CA≃0.

On a statistical basis the CME width seems not to play a relevant role in terms of the peak intensity of the SEE event, as the correlations both for the full sample and well-connected events are weak. We note that we found slightly higher correlations between the peak intensities and the CME width estimated as in Dumbović et al. (2019) that takes the tilt of the CME into account (Pearson: cc=0.21±0.04 for the full sample, cc=0.26±0.04 for the well-connected events), than the face-on width of the CME (Pearson: cc=0.11±0.05, cc=0.16±0.05, not shown). In the case of the spectral indices, on top of the large uncertainties, we suspect that the missing correlations might be partly due to a selection effect, as MESSENGER is mostly measuring large events, the majority of them being widely spread in the heliosphere and with the presence of relativistic electron enhancements. The spectral indices in the MESSENGER sample are mainly hard, with a mean δ200=-1.9±0.3, as can be observed in Fig. 4, while SEE spectra in general can be much softer (e.g. Dresing et al. 2020).

6.2.3. Other quantities affecting the peak intensities

The conditions of particle acceleration and propagation in the high corona and interplanetary space affect SEP intensities. The asymmetry in the positive and negative angles delimiting the subsample of events with the highest peak intensities might be associated to several processes. A possible scenario could be related to acceleration mechanisms in the shock environment at a certain height from the Sun and the evolution of magnetic field connection to the shock front (e.g. Lario et al. 2014; Ding et al. 2022), where the maximum peak intensity is observed when the flare occurs eastward of the spacecraft magnetic footpoint. For example, the nominal best connection to a source at W60 is modified by a CME-driven shock that moves out radially so that the connection to its apex is more towards the east than W60. Perpendicular diffusion processes during the transport of SEPs in the heliosphere might also be related to this asymmetry (e.g. He & Wan 2015).

The pre-event intensity level might also play a role. Figure 2b shows that, for the well-connected events (purple points), the peak SEE intensities associated to a CME-driven shock of a given speed vary over ~4 orders of magnitude, similar to the result found by Kahler (2001), who used pre-event background-subtracted SEE peak intensities. This could be interpreted as evidence for a supra-thermal seed population that made local shock acceleration more efficient. Other related factors to observing a range of peak intensities for a given speed might be the dynamic connection between MESSENGER and the traveling shock; and the presence of previous disturbances in the IP space that may affect the interplanetary magnetic-field structure in which SEEs propagate. Furthermore, as MESSENGER lacks solar wind measurements, the magnetic separation angle, determined with an assumed solar wind speed of 400 km/s, could deviate significantly. We also clearly observe in this study that the poor connectivity to the solar source blurs the correlation between the peak intensities and the solar activity. This might be related to the poorly-connected events being affected by transport effects and/or to the connection to weaker parts of a shock, as discussed in Sect. 6.2.2.

6.3. Final discussion

The highest correlations found in this study between the near-relativistic electron peak intensities and the solar activity are with the 3D CME-driven shock speed and the flare intensity. This is a statistical confirmation of the idea that both flare and shock-related processes may contribute to the acceleration of near relativistic electrons in large SEE events (Kallenrode 2003; Trottet et al. 2015; Dresing et al. 2022), provided the flare-accelerated particles escape to interplanetary space. The correlations found between the flare intensity and the shock speed being lower than the correlations between the SEE peak intensities and the flare intensity or the shock speed might support this result.

However, we observe several indications in this study that favour a scenario where the relevance of particle acceleration by shock-related mechanisms is larger against the flare-related processes: (1) The majority of the events are accompanied by relativistic electrons. According to Dresing et al. (2022) this would be an evidence of the presence of efficient electron acceleration, which could be related to acceleration in a shock environment.

(2) The asymmetry to the east of the range of connection angles for which the SEE events are presenting higher peak intensities and higher correlations with the solar activity, which could be related to the evolution of the magnetic field connection to the shock front (Lario et al. 2006, 2013; Ding et al. 2022). (3) The ~ 4 orders of magnitude in the SEE peak intensities for the same CME-driven shock speed that might be related to the presence of supra-thermal seed population that made local shock acceleration more efficient. (4) The somewhat higher correlations found in this study between the SEE peak intensities and the shock speed (Pearson: cc=0.65±0.04; Kelly: cc=0.87±0.20; 25 events) versus the flare intensity (Pearson: cc=0.59±0.03; Kelly: cc=0.74±0.30; 19 events). On top of the higher correlations, we find lower uncertainties (Kelly), indicating that the correlation is more significant.

Also, we found a stronger correlation between the SEE peak intensities and the maximum speed of the 3D CME-driven shock than with the 3D CME speed. This means that the maximum acceleration achieved in the CME-related mechanisms, usually observed before 10 $R_\odot$, is a better proxy for the acceleration of particles than the linear estimation of the CME speed based on the height-time profile of the 3D CME apex.

Closer to the Sun (i.e., closer to the acceleration site), we find stronger correlations with the solar parameters associated to the electron acceleration mechanisms in comparison with previous studies using near 1 au data. This difference is more relevant when comparing studies with similar connectivity and using the 3D parameters of the CME-related activity (Xie et al. 2019; Dresing et al. 2022). This suggests that the effect of the IP transport from near 0.3 au to near 1 au on the energetic electrons might weaken the correlations between the solar source parameters and the peak intensities measured in situ.

This statistical study of intense SEE events at heliocentric distances near 0.3 au is relevant and timely. The analysis and outcomes presented here might be further investigated with data from the new ongoing missions exploring the innermost regions of the heliosphere, such as *Solar Orbiter* (Müller et al. 2020; Zouganelis et al. 2020), *Parker Solar Probe* (PSP; Fox et al. 2016) and *BepiColombo* (Benkhoff et al. 2010), together with near 1 au missions remotely observing the Sun. Alternative parameters related to the solar activity, such as the SXR fluence, the CME over expansion speed in the early phases close to the Sun surface, and shock characteristics at the cobpoint, which might describe in some sense better the strength of the probable accelerators (Trottet et al. 2015; Dresing et al. 2022), could be also investigated in future studies. By using these new multi-spacecraft observations and as we progress into the solar cycle 25, we will measure more events and increase the statistics, which will allow a reduction of the uncertainties.

Acknowledgements. The UAH team acknowledges the financial support by the Spanish Ministerio de Ciencia, Innovación y Universidades FEDER/MCIU/AEI Projects ESP2017-88436-R and PID2019-104863RB-I00/AEI/10.13039/501100011033 and by the European Union's Horizon 2020 research and innovation program under grant agreement No. 101004159 (SERPENTINE). LRG is also supported by the European Space Agency, under the ESA/NPI program and thanks Karl Ludwig Klein, Angelos Vourlidas and Nariaki Nitta for their help. LAB acknowledges the support from the NASA program NNH17ZDA001N-LWS (Awards Nr. 80NSSC19K0069 and 80NSSC19K1235). AK acknowledges financial support from NASA NNN06AA01C (SO-SIS Phase-E) contract. ND is grateful for support by the Turku Collegium for Science, Medicine and Technology of the University of Turku, Finland and acknowledges the support of Academy of Finland (SHOCKSEE, grant 346902). DL acknowledges support from NASA Living With a Star (LWS) programs NNH17ZDA001N-LWS and NNH19ZDA001N-LWS, and the Goddard Space Flight Center Internal Scientist Funding Model (competitive work package) program and the Heliophysics Innovation Fund (HIF) program. The authors acknowledge the different SOHO, STEREO instrument teams, and the STEREO and ACE science centers for providing the data used in this paper. This research has used PyThea v0.6.6, an open-source and free Python package to reconstruct the 3D structure of CMEs and shock waves (GCS and ellipsoid model).

ORCID iDs

Laura Rodríguez-García https://orcid.org/0000-0003-2361-5510
Laura Balmaceda https://orcid.org/0000-0003-1162-5498
Raúl Gómez-Herrero https://orcid.org/0000-0002-5705-9236
Athanasios Kouloumvakos https://orcid.org/0000-0001-6589-4509
Nina Dresing https://orcid.org/0000-0003-3903-4649
David Lario https://orcid.org/0000-0002-3176-8704
Ioannis Zouganelis https://orcid.org/0000-0003-2672-9249
Annamaria Fedeli https://orcid.org/0000-0001-9449-4782
Francisco Espinosa Lara https://orcid.org/0000-0001-9039-8822
Ignacio Cernuda https://orcid.org/0000-0001-8432-5379
George Ho https://orcid.org/0000-0003-1093-2066
Robert Wimmer-Schweingruber https://orcid.org/0000-0002-7388-173X
Javier Rodríguez-Pacheco https://orcid.org/0000-0002-4240-1115

References

Agueda, N. & Lario, D. 2016, ApJ, 829, 131
Andrews, G. B., Zurbuchen, T. H., Mauk, B. H., et al. 2007, Space Sci. Rev., 131, 523
Bein, B. M., Berkebile-Stoiser, S., Veronig, A. M., Temmer, M., & Vršnak, B. 2012, ApJ, 755, 44
Benkhoff, J., van Casteren, J., Hayakawa, H., et al. 2010, Planet. Space Sci., 58, 2
Brueckner, G. E., Howard, R. A., Koomen, M. J., et al. 1995, Solar Physics, 162, 357
Curran, P. A. 2015, MCSpearman: Monte Carlo error analyses of Spearman's rank test, Astrophysics Source Code Library, record ascl:1504.008
D'Agostino, R. & Pearson, E. S. 1973, Biometrika, 60, 613
Ding, Z., Li, G., Ebert, R. W., et al. 2022, Journal of Geophysical Research: Space Physics, 127, e2022JA030343, e2022JA030343 2022JA030343
Domingo, V., Fleck, B., & Poland, A. I. 1995, Sol. Phys., 162, 1
Dresing, N., Effenberger, F., Gómez-Herrero, R., et al. 2020, ApJ, 889, 143
Dresing, N., Gómez-Herrero, R., Heber, B., et al. 2014, Astrophysical Journal, 567, A27
Dresing, N., Kouloumvakos, A., Vainio, R., & Rouillard, A. 2022, ApJ, 925, L21
Dresing, N., Theesen, S., Klassen, A., & Heber, B. 2016, A&A, 588, A17
Dumbović, M., Guo, J., Temmer, M., et al. 2019, ApJ, 880, 18
Feigelson, E. D. & Babu, G. J. 2012, Modern Statistical Methods for Astronomy (Cambridge University Press)
Fox, N. J., Velli, M. C., Bale, S. D., et al. 2016, Space Sci. Rev., 204, 7
García, H. A. 1994, Sol. Phys., 154, 275
Gieseler, J., Dresing, N., Palmroos, C., et al. 2022, Frontiers in Astronomy and Space Physics, (submitted)
Gieseler, J., Dresing, N., Palmroos, C., et al. 2022, arXiv e-prints, arXiv:2210.00819
He, H. Q. & Wan, W. 2015, ApJS, 218, 17
Heras, A. M., Sanahuja, B., Lario, D., et al. 1995, ApJ, 445, 497
Howard, R. A., Moses, J. D., Vourlidas, A., et al. 2008, Space Sci. Rev., 136, 67
Kahler, S., Burkepile, J., & Reames, D. 1999, in International Cosmic Ray Conference, Vol. 6, 26th International Cosmic Ray Conference (ICRC26), Volume 6, 248
Kahler, S. W. 1982, J. Geophys. Res., 87, 3439
Kahler, S. W. 2001, J. Geophys. Res., 106, 20947
Kahler, S. W. 2007, Space Sci. Rev., 129, 359
Kahler, S. W. & Hundhausen, A. J. 1992, J. Geophys. Res., 97, 1619
Kaiser, M. L., Kucera, T. A., Davila, J. M., et al. 2008, Space Sci. Rev., 136, 5
Kallenrode, M. B. 2003, Journal of Physics G Nuclear Physics, 29, 965
Kelly, B. C. 2007, ApJ, 665, 1489
Kihara, K., Huang, Y., Nishimura, N., et al. 2020, ApJ, 900, 75
Klein, K. L., Krucker, S., Trottet, G., & Hoang, S. 2005, A&A, 431, 1047
Kokoska, S. & Zwillinger, D. 2000, CRC Standard Probability and Statistics Tables and Formulae (New York, NY: Springer New York), 502–505

Kouloumvakos, A., Nindos, A., Valtonen, E., et al. 2015, A&A, 580, A80
Kouloumvakos, A., Patsourakos, S., Nindos, A., et al. 2016, ApJ, 821, 31
Kouloumvakos, A., Rodríguez-García, L., Gieseler, J., et al. 2022, Frontiers in Astronomy and Space Sciences, 9
Kouloumvakos, A., Rouillard, A. P., Wu, Y., et al. 2019, ApJ, 876, 80
Kowalski. 1972, Journal of the Royal Statistical Society. Series C (Applied Statistics), 21
Krucker, S., Kontar, E. P., Christe, S., Glesener, L., & Lin, R. P. 2011, ApJ, 742, 82
Kunow, H., Wibberenz, G., Green, G., Müller-Mellin, R., & Kallenrode, M.-B. 1991, in Physics of the Inner Heliosphere II, Vol. 21 (Springer-Verlag), 243–342
Kwon, R.-Y., Zhang, J., & Olmedo, O. 2014, ApJ, 794, 148
Lario, D., Aran, A., Gómez-Herrero, R., et al. 2013, Astrophysical Journal, 767, 41
Lario, D., Ho, G. C., Decker, R. B., et al. 2003, in American Institute of Physics Conference Series, Vol. 679, Solar Wind Ten, ed. M. Velli, R. Bruno, F. Malara, & B. Bucci, 640–643
Lario, D., Kallenrode, M. B., Decker, R. B., et al. 2006, ApJ, 653, 1531
Lario, D., Roelof, E. C., & Decker, R. B. 2014, in Astronomical Society of the Pacific Conference Series, Vol. 484, Outstanding Problems in Heliophysics: From Coronal Heating to the Edge of the Heliosphere, ed. Q. Hu & G. P. Zank, 98
Lemen, J. R., Title, A. M., Akin, D. J., et al. 2012, Sol. Phys., 275, 17
Maia, D. J. F. & Pick, M. 2004, ApJ, 609, 1082
Müller, D., St. Cyr, O. C., Zouganelis, I., et al. 2020, A&A, 642, A1
Nitta, N. V., Aschwanden, M. J., Boerner, P. F., et al. 2013, Sol. Phys., 288, 241
Papaioannou, A., Sandberg, I., Anastasiadis, A., et al. 2016, Journal of Space Weather and Space Climate, 6, A42
Pesnell, W. D., Thompson, B. J., & Chamberlin, P. C. 2012, Sol. Phys., 275, 3
Richardson, I. G., von Rosenvinge, T. T., Cane, H. V., et al. 2014, Solar Physics, 289, 3059
Rodríguez-García, L., Gómez-Herrero, R., Dresing, N., et al. 2022, A&A, (in press)
Rodríguez-García, L., Gómez-Herrero, R., Zouganelis, I., et al. 2021, A&A, 653, A137
Rodríguez-García, L., Nieves-Chinchilla, T., Gómez-Herrero, R., et al. 2022, A&A, 662, A45
Simnett, G. M., Roelof, E. C., & Haggerty, D. K. 2002, ApJ, 579, 854
Solomon, S. C., McNutt, R. L., Gold, R. E., & Domingue, D. L. 2007, Space Sci. Rev., 131, 3
Spearman, C. 1987, The American Journal of Psychology, 100, 441
Stephens, M. A. 1974, Journal of the American Statistical Association, 69, 730
Stone, E. C., Frandsen, A. M., Mewaldt, R. A., et al. 1998, Space Sci. Rev., 86, 1
Thernisien, A. 2011, ApJS, 194, 33
Thernisien, A., Vourlidas, A., & Howard, R. A. 2009, Solar Physics, 256, 111
Thernisien, A. F. R., Howard, R. A., & Vourlidas, A. 2006, ApJ, 652, 763
Trottet, G., Samwel, S., Klein, K. L., Dudok de Wit, T., & Miteva, R. 2015, Sol. Phys., 290, 819
Wall, J. V. & Jenkins, C. R. 2003, Practical Statistics for Astronomers, Vol. 3 (Cambridge University Press)
West, S. G., Finch, J. F., Curran, P. J., & Hoyle, R. 1995, Structural equation models with nonnormal variables: Problems and remedies, 55
Wuelser, J.-P., Lemen, J. R., Tarbell, T. D., et al. 2004, in Society of Photo-Optical Instrumentation Engineers (SPIE) Conference Series, Vol. 5171, Telescopes and Instrumentation for Solar Astrophysics, ed. S. Fineschi & M. A. Gummin, 111–122
Xie, H., St. Cyr, O. C., Mäkelä, P., & Gopalswamy, N. 2019, Journal of Geophysical Research (Space Physics), 124, 6384
Yashiro, S., Gopalswamy, N., Michalek, G., et al. 2004, Journal of Geophysical Research (Space Physics), 109, A07105
Zhang, J., Dere, K. P., Howard, R. A., & Vourlidas, A. 2004, ApJ, 604, 420
Zouganelis, I., De Groof, A., Walsh, A. P., et al. 2020, A&A, 642, A3

Appendix A: Solar energetic electron events measured by the MESSENGER mission

Table A.1. Solar energetic electron events measured by MESSENGER.

#	Solar event			CME parameters		Shock			SEE event	
	Date	T-III onset (UT ± 5 min)	Flare loc [class] (deg)	speed (GCS) (km s^{-1})	width (deg)	speed (3D) (km s^{-1})	CA MESS (deg)	R MESS (au)	I_{max_MESS} (bg) 71 to 112 keV e (cm^2 sr s MeV)$^{-1}$	δ MESS (-)
(1)	(2)	(3)	(4)	(5)	(6)	(7)	(8)	(9)	(10)	(11)
*1	2010/08/14	10:00^	N17W052 [C4.4]	960	64	1631	-67	0.31	2.5×10^4 (1.6×10^4)	-
*2	2010/08/18	05:35	N17W101 [C4.5]	1634	57	1781	-39	0.31	3.7×10^4 (1.5×10^4)	-
*3	2011/03/07	19:55^	N30W048 [M3.7]	2250	51	2505	168	0.34	7.5×10^4 (1.6×10^4)	-1.78±0.13†
*4	2011/06/04	06:50	N16W144 [-]	1086	106	1826	-12	0.33	3.1×10^4 (9.0×10^3)	-2.26±1.14
*5	2011/06/04	21:50^	N16W153 [-]	2200	126	3397	-5	0.33	4.9×10^7 (2.0×10^4)	-1.94±0.21†
*6	2011/08/02	06:25^	N15W015 [M1.4]	807	90	1114	19	0.46	1.5×10^3 (2.5×10^2)	-
*7	2011/08/04	03:50	N19W036 [M9.3]	1125	88	2572	37	0.46	1.6×10^3(5.0×10^2)	-
*8	2011/09/22	10:40	N09E089 [X1.4]	1300	81	2206	90	0.36	8.1×10^4 (1.4×10^4)	-1.97 ±0.36†
*9	2011/10/04	12:30^	N26E153 [-]	1358	77	1341	-14	0.42	2.9×10^5 (1.0×10^4)	-1.88±0.17†
10	2011/10/14	11:00^	N10E140 [-]	889	74	1166	-36	0.47	2.3×10^4 (1.2×10^4)	-
*11	2011/11/03	22:15	N09E154 [-]	890	76	1210	-74	0.44	1.4×10^5 (9.0×10^3)	-1.69±0.10†
12	2011/11/09	13:10	N24E035 [M1.1]	1133	45	1446	34	0.42	3.6×10^4 (1.0×10^4)	-1.96±0.28†
*13	2011/11/17	20:15^	N18E120 [-]	948	106	1254	-71	0.38	5.8×10^4 (7.1×10^3)	-1.94±0.26†
*14	2012/01/02	14:30	N08W104 [C2.4]	1125	83	1443	-34	0.43	2.1×10^4 (8.1×10^3)	-
*15	2012/01/23	03:40	N28W021 [M8.7]	1775	91	2014	-157	0.46	3.4×10^4 (8.7×10^3)	-1.78±0.36†
*16	2012/01/27	18:15	N27W078 [X1.7]	1750	70	2468	-108	0.46	8.7×10^4 (8.5×10^3)	-1.70±0.19†
*17	2012/03/04	11:05	N19E061 [M2.0]	1588	46	1497	-8	0.31	8.4×10^4 (8.9×10^3)	-2.41±1.29†
*18	2012/03/05	03:35	N17E052 [X1.1]	850	72	2231	-2	0.31	1.5×10^6 (4.1×10^4)	-1.98±0.20†
*19	2012/03/07	00:20	N17E027 [X5.4]	2700	71	3303	13	0.31	2.2×10^7 (1.9×10^4)	-2.02±0.26†
*20	2012/05/17	01:30	N11W076 [M5.1]	1458	75	1807	-76	0.35	8.7×10^4 (2.0×10^4)	-
*21	2012/05/26	20:40	N15W116 [-]	1850	55	2665	-80	0.31	1.9×10^4 (4.0×10^3)	-1.70±0.53
*22	2012/05/27	05:10^	S10E054 [C3.1]	1052	78	958	108	0.31	1.3×10^5 (2.4×10^4)	-2.56±0.96†
*23	2012/07/12	15:45^	S15W001 [X1.4]	1393	75	1617	4	0.46	1.1×10^6 (5.5×10^3)	-1.95±0.27†
24	2012/07/17	14:00^	S20W065 [C9.9]	821	50	1245	59	0.46	1.6×10^4 (2.8×10^3)	-
25	2012/07/19	05:20	S13W088 [M7.7]	1500	71	1897	79	0.46	2.6×10^4 (7.1×10^3)	-
*26	2012/07/23	02:10^	S17W132 [-]	1900	116	2520	116	0.45	5.8×10^4 (9.5×10^3)	-1.90±0.18†
27	2012/07/28	21:05	S25E055 [M6.1]	792	68	1255	-76	0.44	5.4×10^4 (4.7×10^3)	-2.11±0.42†
*28	2012/09/20	14:55	S15E155 [-]	2600	54	3353	-29	0.42	2.0×10^6 (2.5×10^4)	-1.91±0.21†
*29	2012/10/14	00:35	N13E137 [-]	1200	61	1502	-58	0.46	1.9×10^5 (4.0×10^3)	-1.93±0.15†
30	2013/03/16	05:45	S15W045 [C2.8]	260	61	-	-14	0.43	2.7×10^5 (5.0×10^4)	-1.92±0.45†
*31	2013/04/11	07:00	N09E012 [M6.5]	1350	130	1602	-122	0.46	2.2×10^4 (2.7×10^3)	-
32	2013/04/24	21:40	N10W175 [-]	560	73	1017	38	0.40	3.3×10^6 (7.6×10^3)	-2.22±0.16†
*33	2013/05/13	15:55	N11E085 [X2.8]	2000	84	2308	67	0.31	2.4×10^4 (6.3×10^3)	-1.80±0.59
*34	2013/06/21	02:50^	S16E073 [M2.9]	1428	60	2303	-67	0.46	5.5×10^5 (4.7×10^3)	-1.82±0.30†
35	2013/08/19	01:20^	N10W162 [-]	-	-	-	-13	0.32	4.0×10^4 (1.5×10^4)	-
*36	2013/08/19	22:30	N08W178 [M3.3§]	1149	118	1192	-1	0.32	2.9×10^7 (1.0×10^4)	-1.99±0.25†
*37	2013/10/11	07:10	N21E103 [M1.5]	875	160	1267	-56	0.43	1.4×10^5 (4.6×10^3)	-1.92±0.08†
*38	2013/10/25	08:00	S10E073 [X1.7]	500	65	1188	-62	0.36	2.2×10^5 (1.3×10^4)	-1.85±0.16†
*39	2013/10/25	15:00	S06E069 [X2.1]	1225	69	1686	-59	0.36	2.8×10^5 (5.4×10^4)	-1.89±0.18†

(Continued on next page.)

Table A.1. (continued.)

#	Solar event			CME parameters		Shock			SEE event	
	Date	T-III onset (UT ± 5 min)	Flare loc [class] (deg)	speed (GCS) (km s^{-1})	width (deg)	speed (3D) (km s^{-1})	CA MESS (deg)	R MESS (au)	I_{max_MESS} (bg) 71 to 112 keV e (cm^2 sr s MeV)$^{-1}$	δ MESS (-)
(1)	(2)	(3)	(4)	(5)	(6)	(7)	(8)	(9)	(10)	(11)
*40	2013/10/28	15:10	S08E028 [M4.4]	1400	56	1393	-29	0.34	8.1×10^5 (2.1×10^4)	-1.97±0.06†
*41	2013/11/19	10:25	S15W069 [X1.0]	1138	52	1361	-41	0.34	6.2×10^4 (5.4×10^4)	-1.93±0.31†
*42	2013/11/30	05:10$^\wedge$	N13W150[-]	-	-	-	2	0.40	1.5×10^4 (4.9×10^3)	-
*43	2013/11/30	15:00$^\wedge$	S15E146 [-]	830	48	830	65	0.40	1.6×10^4 (8.2×10^3)	-
*44	2013/12/26	03:05	S09E166 [-]	1738	47	1753	-9	0.46	1.1×10^6 (4.2×10^3)	-2.02±0.38†
*45	2014/01/07	18:05	S15W011 [X1.2]	2190	61	2486	145	0.43	3.2×10^4 (6.1×10^3)	-
*46	2014/01/28	00:30$^\wedge$	S10E081 [C7.6]	-	-	-	-8	0.32	5.9×10^3 (8.1×10^2)	-
47	2014/01/28	05:25$^\wedge$	S14E088 [C9.3]	-	-	-	-16	0.32	2.2×10^4 (2.7×10^3)	-2.02±1.02†
48	2014/01/30	16:05	S13E058 [M6.6]	1450	66	1367	2	0.31	7.4×10^4 (7.1×10^3)	-1.82±0.33†
49	2014/02/20	07:50	S15W073 [M3.0]	1103	70	1328	34	0.37	1.3×10^4 (1.5×10^3)	-
*50	2014/02/25	00:45	S12E082 [X4.9]	2350	69	2431	-137	0.40	5.5×10^4 (1.2×10^3)	-1.91±0.47†
*51	2014/03/13	21:40$^\wedge$	N15W140 [-]	498	23	803	81	0.46	2.3×10^4 (3.8×10^3)	-1.55±0.31
52	2014/08/08	16:15	S10W160 [-]	1035	57	1352	-41	0.33	7.3×10^4 (6.2×10^3)	-1.82±0.21†
*53	2014/09/01	11:00	N14E127 [-]	1842	77	2947	-44	0.45	2.9×10^7 (3.4×10^3)	-1.81±0.03†
54	2014/09/05	06:50	S14E069 [C6.8]	565$^!$	56$^!$	NP	6	0.46	8.6×10^4 (3.9×10^4)	-2.06±0.65
55	2014/09/08	23:55	N12E029 [M4.5]	1120	36	1077	39	0.47	2.6×10^4 (5.4×10^3)	-
*56	2014/09/10	17:30	N14E002 [X1.6]	1580	74	1427	64	0.47	5.6×10^4 (1.0×10^4)	-1.77±0.16†
*57	2014/09/24	20:45	N13E179 [-]	1516	76	1651	-139	0.44	5.3×10^4 (4.7×10^3)	-2.19±0.13†
58	2014/12/13	14:05$^\wedge$	S20W143 [-]	2036$^!$	92$^!$	2519$^!$	-75	0.46	7.8×10^6 (3.4×10^3)	-1.92±0.26†
59	2015/02/21	09:30$^\wedge$	S40W075 [B4.8]	884$^!$	65$^!$	1088$^!$	-19	0.44	3.8×10^4 (3.9×10^3)	-
60	2015/03/24	08:30$^\wedge$	S01W121 [-]	1371$^!$	106$^!$	2102$^!$	-31	0.43	1.2×10^6 (1.3×10^4)	-1.94±0.24†
*61	2015/04/14	09:15$^\wedge$	S15W100 [B9]	484$^!$	31$^!$	NP	-119	0.32	1.5×10^4 (4.5×10^3)	-

Notes. Columns 1 and 2: Event number and date. Column 3: Type III radio burst onset time. Column 4: Flare location in Stonyhurst coordinates and flare class based on GOES Soft X-ray (SXR) peak flux. Column 5: 3D CME speed at the apex based on the GCS analysis. Column 6: 3D CME width at the equatorial plane based on the GCS reconstructed CME parameters, as in Dumbović et al. (2019). Column 7: 3D CME-driven shock maximum speed at the apex based on the ellipsoid model (Kwon et al. 2014). Column 8: Longitudinal separation between the flare location and the footpoint of the magnetic field line connecting to MESSENGER, based on a 400 km s^{-1} Parker spiral (positive connection angle (CA) denotes a flare source located at the western side of the spacecraft magnetic footpoint). Column 9: MESSENGER radial distance from the Sun. Column 10: 71 -112 keV electron peak intensity measured by MESSENGER. The pre-event background level is shown in parenthesis. Column 11: Spectral index of peak intensities based on 71 keV to 1 MeV energies. * in Col. 1: Widespread SEP event, namely when MESSENGER |CA| or |CA difference| with near 1 au spacecraft is ≥80°. $^\wedge$ in Col. 3: Type III radio burst onset time is uncertain due to occultation or multiple radio emission at the same time during the onset of the event. § in Col. 4: The GOES intensity level is deduced from the STEREO/EUVI light curve as explained in Rodríguez-García et al. (2021). NP in Cols. 5-7: not possible to reconstruct. $^!$ in Cols. 5-7: CME and CME-driven shock reconstructions using only LASCO and SDO data. † in Col. 11: Presence of ∼1 MeV electrons.